Magnetic and magnetotransport properties of a Co–Sn evaporated trilayer

2008 J. Phys.: Condens. Matter 20 345213

(http://iopscience.iop.org/0953-8984/20/34/345213)

J. Phys.: Condens. Matter **20** (2008) 345213 (9pp) doi:10.1088/0953-8984/20/34/345213

Magnetic and magnetotransport properties of a Co–Sn evaporated trilayer

A Chiolerio[1], P Allia[1], P Tiberto[2] and M Coïsson[2]

[1] Physics Department, Politecnico di Torino, Corso Duca degli Abruzzi 24, I-10129 Torino, Italy
[2] Electromagnetism Division, Istituto Nazionale di Ricerca Metrologica, Strada delle Cacce 91, I-10135 Torino, Italy

Received 26 November 2007, in final form 20 June 2008
Published 1 August 2008
Online at stacks.iop.org/JPhysCM/20/345213

Abstract

The aim of this work is the magnetic characterization of a Co–Sn–Co trilayer produced by thermal evaporation. Magnetization and magnetotransport measurements performed at low temperatures show that the sample has a complex behaviour related to the different morphologies of the external Co layers. A fitting procedure is introduced to disentangle the magnetization behaviour of different regions of the trilayer; three magnetic phases can be seen. Likewise, the magnetoresistance (MR) curves show the superposition of three different effects: a low-field positive MR, a slowly saturating negative MR similar to the one measured in granular systems, and an ordinary MR which becomes significant at very low temperatures. Combining magnetic and magnetotransport data, the three magnetic phases have been associated with the continuous Co underlayer, to the corrugated Co cap layer and to nanometre-sized Co islands embedded in the Sn layer (respectively). The three-phase model coherently explains both magnetization and magnetoresistance datasets. A simple MR model based on a resistance network has been created to fit the experimental data; the fit is shown to match the main features of the experimental MR.

(Some figures in this article are in colour only in the electronic version)

1. Introduction

Layered structures containing one or more ferromagnetic metals have gained much interest during the last decades owing to the remarkable development of spintronics in metals, which has given rise to a variety of devices such as spin valves, pseudo-spin valves and magnetic tunnel junctions of different geometries [1–4]. One of the simplest and most popular spintronic devices not involving semiconductors is the spin valve [3], based on the basic stacking FM/NM/FM, where FM is a ferromagnetic metal or alloy and NM is a non-magnetic metal; in giant magnetoresistance (GMR) multilayers the interlayer exchange coupling provides stability for either a parallel or antiparallel magnetization configuration in the two FM layers, depending on the thickness of the NM spacer [5]. In this paper, the magnetic and magnetotransport properties of a non-standard layered structure prepared through thermal evaporation and composed of two ferromagnetic layers of Co intercalated by a diamagnetic layer of Sn are studied in detail. Both the difference in atomic radii between these two metallic species and the preparation technique point to a particularly high interfacial roughness and to possible intermixing effects, which make this system interesting from the viewpoint of basic research, owing to the variety of magnetic and magnetoresistance (MR) effects which can simultaneously occur at all temperatures.

A morphological and compositional survey of the properties of this material has been submitted elsewhere [6]. An accurate procedure which involves combined processing of images obtained by field-emission scanning electron microscopy (FESEM) and energy-dispersive x-ray analysis (EDX) indicates that the bottom Co film directly grown on Si is flat and homogeneous, while the Sn interlayer shows a Stranski–Krastanov growth mechanism [7] and an island-like appearance. As a consequence, the Co cap film becomes extremely corrugated and possibly not continuous. This peculiar structure greatly affects all physical properties; in particular, magnetization curves and magnetotransport data will be discussed here in the light of the structural information extracted from the previous morphological analysis.

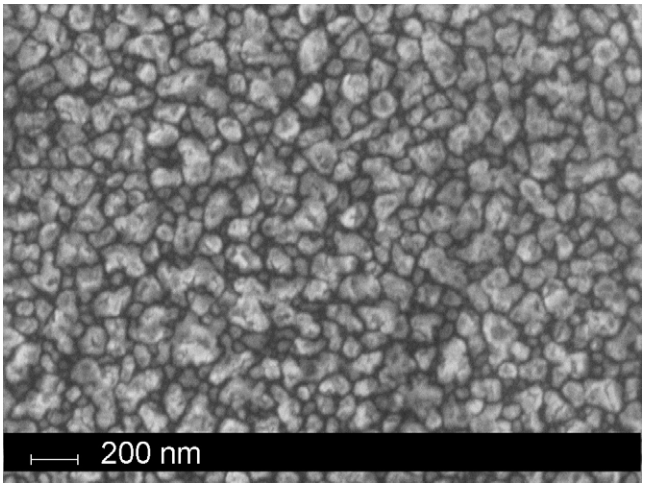

Figure 1. FESEM image of the sample surface (resolution: 0.385 nm/px).

2. Experimental details

The sample was prepared as described in detail elsewhere [6]; here, a brief summary follows.

The multilayered structure has been thermally evaporated at room temperature with a base pressure of 3×10^{-8} Torr on clean Si(100) substrates using very high purity raw materials (>99.99%) as evaporating sources. The stacking structure was Co 20 nm/Sn 45 nm/Co 15 nm, where the spacer thickness refers to its maximum value. The morphological characterization was done by FESEM and EDX spectroscopy on the same specimen regions, with very high lateral resolution (0.385 nm/px for FESEM images and 2.5 nm/px for EDX micromaps, as shown in [6]). A numerical algorithm combining FESEM and EDX micromaps was implemented to obtain accurate information about the distribution of Co and Sn, as described in [6].

Magnetic hysteresis loops were measured from 8 to 300 K in an alternating gradient field magnetometer (magnetic field range up to ∼18 kOe) with H applied in the plane of the layers. The magnetic signal was corrected for the contributions coming from the sample holder and substrate.

MR measurements were performed in the current-in-plane configuration by means of the conventional four-contact technique with soldered contacts in a superconducting magnet (temperature range: 2–121 K; magnetic field range: up to 70 kOe). Suitable specimens for magnetoresistance measurements were obtained by shadow masking of evaporated films as 20 mm × 4 mm stripes; Cu ohmic contacts were subsequently evaporated through other stripes as thick 500 nm films on top of the stack; external leads were soldered using an In/Sn alloy. The in-plane magnetic field was applied parallel to the current. In this work, the MR is defined as

$$\mathrm{MR} = \frac{R(H) - R_{\mathrm{Max}}}{R_{\mathrm{Max}}} \times 100, \qquad (1)$$

where R_{Max} is the maximum value of the electrical resistance.

3. Results

An example of the sample morphology is shown in figure 1: the island-like growth of evaporated regions is apparent, as well as an additional granularity on a smaller scale.

Magnetization loops measured on the Co/Sn trilayer are shown in figures 2(a) and (b).

At low temperatures, a non-saturating behaviour of the $M(H)$ curves becomes apparent. The low-field region is expanded in figure 2(b); the loops are symmetrical around $H = 0$ and exhibit a characteristic bending distinctive of a multi-phase behaviour. The temperature merely changes some details of the curve without affecting its general features. The coercive field steadily decreases with increasing temperature; the average magnetic susceptibility at coercivity shows a regularly growing trend, related to the gradual shrinking and steepening of hysteresis loops; in a similar way, the susceptibility at remanence increases also. In contrast, the high-field susceptibility is steadily reduced with increasing temperature.

Representative MR curves measured on the trilayer are shown in figures 3(a) and (b).

Three different MR effects can be singled out. At very low fields ($H \ll 1$ kOe) and at all temperatures, the resistance

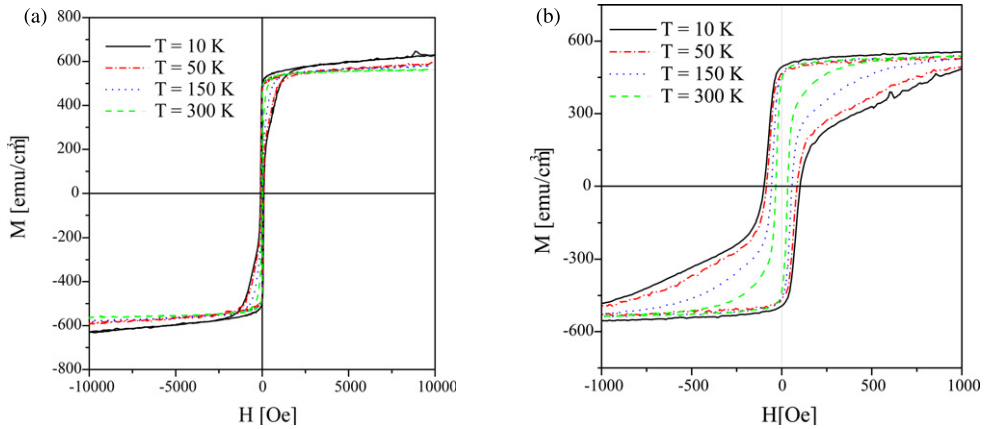

Figure 2. (a) Hysteresis loops measured at different temperatures (10–300 K) up to 10 kOe; (b) magnification of the hysteresis loops at low field.

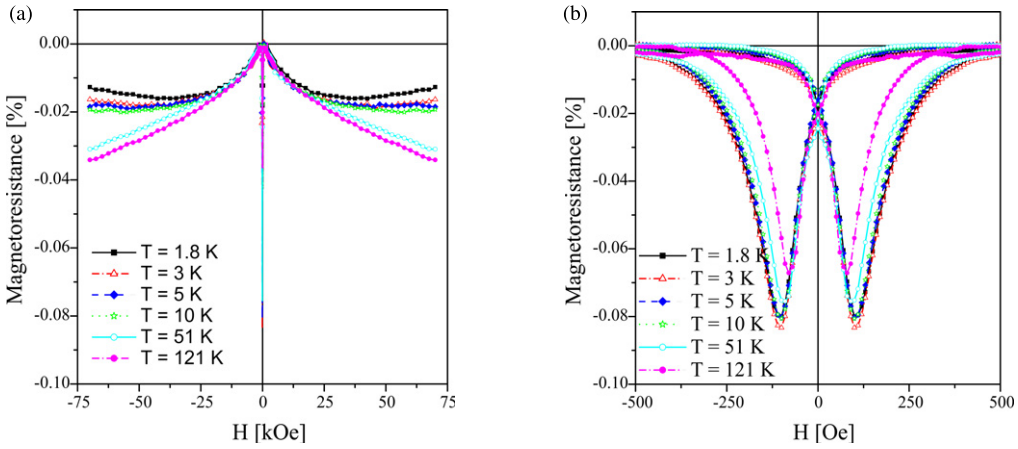

Figure 3. (a) Magnetoresistance curves at different temperatures (1.8–121 K) up to 70 kOe; (b) magnification of the magnetoresistance curves around $H = 0$.

symmetrically increases from a minimum located at about ±120 Oe. This MR effect will be called 'positive' even if its minimum is not coincident with $H = 0$. Figure 3(b) provides a magnification of the resulting resistive dip, whose depth and width decrease with increasing T. At higher fields, a negative unsaturating magnetoresistance is observed; although in the intermediate-field region ($1 \leqslant H \leqslant 20$ kOe) all curves are superimposed, they become separate at very high fields owing to a second positive magnetoresistance effect, which is strongly temperature-dependent, becoming predominant below 10 K.

4. Analysis of magnetization measurements

The measured hysteresis loops indicate that the material cannot be treated as magnetically homogeneous. The unsaturating trend of the $M(H)$ curves and the bending of the loop branches above coercivity suggest that at least three different magnetic phases must be present. An attempt has been made to disentangle these contributions from the experimental curves, singling out their behaviour with magnetic field and temperature. The analysis is substantiated by the fact that the material itself is inhomogeneous, being composed of two Co layers having comparable thicknesses, but very different in planarity and roughness, separated by a thick, island-like Sn layer where Co atoms or clusters can diffuse during deposition. Although the procedure will be based upon ad hoc fitting functions, the results will be shown to match with the magnetoresistance data, thereby validating the procedure itself.

The main assumption is that the contributions of the three phases merely add up to give the total magnetization. This is justified by the actual nature of the considered trilayer, whose magnetic response is expected to come from well-defined, spatially separated regions. In order to model the magnetization loops, use has been made of the superposition of three modified Langevin functions of the type

$$M_{\pm}(H) = \sum_{i=1}^{3} A_i L\,(\alpha_i H \pm \beta_i), \qquad (2)$$

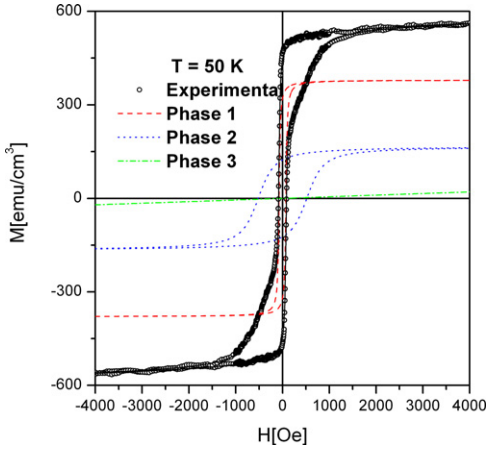

Figure 4. Symbols: experimental $M(H)$ curve measured at 50 K; discontinuous lines: the three corresponding magnetic contributions obtained through the proposed fitting model; solid line (superimposed on experimental data): sum of the three contributions.

where the subscript ± represents the upper (lower) branch of the loop, and A_i, α_i and β_i are fitting parameters. Actually, using the fitting function (2) is justified by its simplicity: the Langevin functions are a much more flexible tool to model the shape of experimental curves. The choice does not imply considering the three magnetic phases as independent, because these Langevin functions have no direct physical meaning. Using three functions means that we postulate (a) the existence of three (interacting) magnetic phases and (b) that there are no additional phases nor additional interactions among them.

Of course, no direct physical meaning can be attributed to the parameters α_i and β_i while the A_i's are the (unnormalized) weights of each magnetic phase, and the ratio $\pm\beta_i/\alpha_i$ is the coercivity of the ith phase. As it turns out, the fits of the experimental curves to equation (2) are good, as shown in figure 4, where the experimental loop at $T = 50$ K (open symbols) is reported together with the corresponding fit to equation (2) (solid black line) and with the contributions from the three magnetic phases (discontinuous lines) whose sum

provides the overall experimental curve. In spite of the linear behaviour of the contribution from phase 3, as apparent in figure 4, the weight A_3 was determined because the fit was done on the whole interval (-18 kOe $< H <$ 18 kOe), where the corresponding Langevin function deviates from linearity. Basically, phase 1 exhibits low coercivity and a fast-saturation behaviour; phase 2 displays a higher coercive field with a rather fast saturation; phase 3 has negligible, or zero, coercivity and describes the unsaturating tail of the $M(H)$ curve at high fields. Although the minor details of the magnetization curves for the three phases are supposed to be dependent on the choice of the fitting function, two sets of parameters, i.e. the coercivities and the relative amplitudes of each component, are believed to be virtually independent of the fitting function used.

The overall coercivity of the trilayer is mostly given by the softer loop (phase 1), which provides the greatest contribution to total magnetization as well; instead, the change in slope of the $M(H)$ curve is related to the harder contribution (phase 2).

In our opinion, phase 1 basically represents the contribution of the continuous Co underlayer, having a fast-saturating response typical of a uniform thin film and exhibiting a coercivity similar to those found in the literature for Co films having similar thickness [8]. A similar coercivity has been observed by us on a Co/Cu/Co trilayer (thicknesses: Co cap layer 5 nm, Cu continuous interlayer: 2 nm; Co underlayer: 15 nm) produced by evaporation under closely similar conditions (see below). Phase 2 is identified as the contribution from the corrugated Co cap layer, whose disordered structure results in a harder response with higher coercivity. The slowly saturating phase 3 could be associated with either dispersed Co clusters/nanoparticles in Sn, or with a magnetically frustrated fraction of magnetic moments present in the corrugated cap layer (as already found, for example, in a Co–Cu thermally evaporated multilayer [9]). In order to get further insight into these phases, it is possible to check the temperature behaviour of their normalized weights $A_i/\Sigma_j A_j$, as reported in figure 5. The weight of phase 3 monotonically decreases with T, with a steeper slope at low temperatures, while just the opposite behaviour is observed for phase 1.

Our analysis suggests a transfer of magnetization from phase 3 to phase 1 (and, to a lesser extent, to phase 2) when the temperature is increased from 2 K up to about 100 K, which indicates that phase 3 is somewhat interacting with the two Co layers. The effect can be explained as follows: phase 3 is constituted by small ferromagnetic particles (or clusters) which are generated during deposition of both the Sn island-like spacer on the Co underlayer and the Co cap layer on top of Sn islands, for reasons connected to the minimization of the surface energy of Sn which may show a surfactant behaviour as In, Ag and Pb show [10]. These Co particles are therefore embedded in the grown Sn islands at a short distance from both Co layers, considering the thicknesses of the evaporated materials. They behave as blocked nanoparticles at low temperatures, with a strong magnetic disorder and a low magnetic susceptibility which explains the unsaturating character of both magnetization and magnetoresistance. When the temperature is increased, some of them gradually unblock, without becoming superparamagnetic because they feel a dipolar interaction with the adjacent phases 1 and 2, so that their magnetic behaviour is finally driven by them. Examples of a similar interplay between a nanoparticulate and a continuous magnetic phase exist (as in [11]). Globally this results in an increase of the fraction of magnetization signal ascribed to phases 1 and 2. Above 100 K, the weight of phase 1 appears to slightly increase, while that of phase 2 decreases, possibly because of cross-talk between the Co underlayer and Co cap layer, mediated by the nanoparticles.

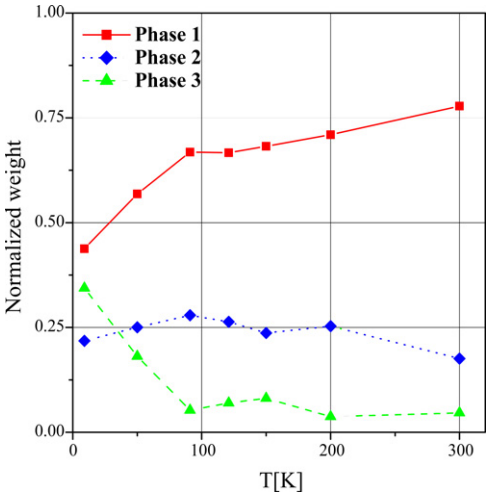

Figure 5. Normalized weights of the three magnetic phases as functions of temperature.

5. Magnetoresistance analysis

MR measurements can be interpreted in the light of the three-phase model. The presence of a non-saturating magnetic phase is clearly associated with the strong negative MR effect observed above 1 kOe, which closely resembles the GMR arising from ordering nanoparticles [5, 12]. In spite of the small weight of phase 3, the negative MR is by no means marginal in our magnetoresistance curves, indicating that the length scale of the magnetic disorder arising from Co nanoparticles is not very different from the electron mean free path [5, 12]. However, the GMR effect is masked (particularly at low temperatures) by a positive MR contribution which is ascribed to an ordinary magnetoresistance (OMR) of all metals constituting the trilayer. The two effects cannot be easily disentangled, and the OMR can well be present—even if with a reduced magnitude—at high temperatures (T = 51 and 121 K). As a consequence, it is not possible to directly check if the GMR-like signal increases with decreasing T, as expected on the basis of the considerations about the number of slowly magnetizing Co nanoparticles constituting phase 3.

The positive magnetoresistance giving rise to the dip shown in figures 3(a) and (b) is most probably related to anisotropic magnetoresistance (AMR) in the continuous Co film. In fact, the thickness of the Co underlayer is compatible with the existence of wide Néel domain walls (>100 nm) in the unmagnetized state [13]. The magnetization vector field

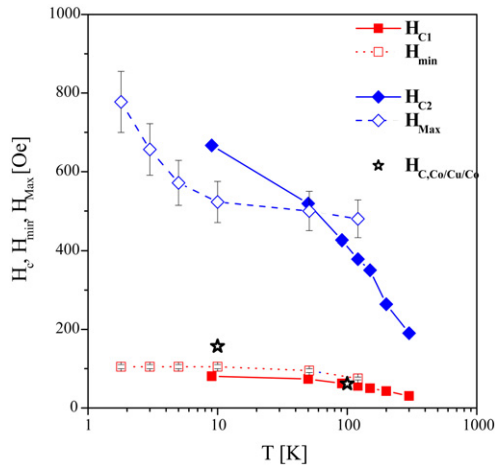

Figure 6. Open symbols: field values corresponding to the minimum or the maximum of MR curves (evaluated from raw MR data; absolute error bar reported); full symbols: coercive fields of magnetic phases 1 and 2 (extracted from magnetization fitting model), plotted at different temperatures. Stars: representative coercivity values of an evaporated Co/Cu/Co trilayer.

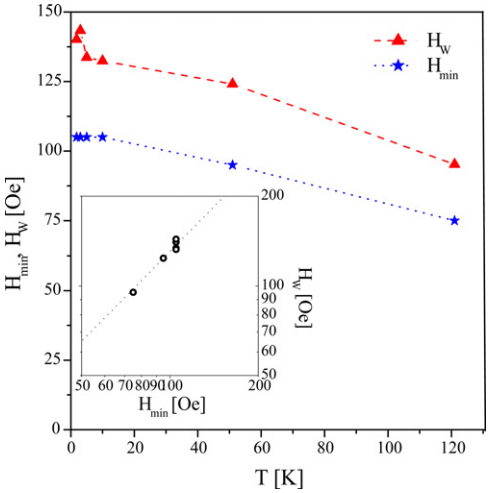

Figure 7. Stars: full width at half-maximum of the low-field MR dip; triangles: field corresponding to the resistance minimum as functions of temperature; their linear correlation is given in the logarithmic plot of the inset.

has a non-zero component perpendicular to the current density vector due to the presence of multidomains; the resistivity minimum around $H = 0$ should correspond to the maximum density of Néel domain walls within phase 1, i.e. to the coercivity of the underlayer.

The coercive fields H_{C1} and H_{C2} for phases 1 and 2 are shown in figure 6 (full symbols). For comparison we show in the same figure the field corresponding to the resistivity dip and the field at which the maximum of the $R(H)$ curve occurs. The low-field magnetoresistance behaviour, including the resistance dip (figure 3(b)) and the intermediate-field resistance maximum, has been the subject of detailed analysis. The raw data have been re-sampled in order to give more accurate numerical computations about the full width at half-maximum of the resistance dip (H_w), the field at which resistive minima occur ($H_{\min}$) and the field at which resistive maxima occur (H_{Max}). Magnetoresistance minima were tracked by means of the first derivative $\mathrm{d}R/\mathrm{d}H$. $H_{\min}$ was computed as the geometrical mean of the field values read correspondingly with the local minima for each sorting direction of the derivatives. H_w was computed making use of a linear fitting function giving the field value corresponding to the half-maximum resistance. The resistive maximum was determined computing a fit of experimental data, using Savitzky–Golay finite impulse response (SGFIR) polynomial functions and then calculating the first numerical derivative of the fit.

The quantities $H_{\min}$ and H_{Max} are reported in figure 6 as functions of temperature. The field $H_{\min}$ corresponds indeed to the coercivity of the underlayer. The agreement may be viewed as proof of the validity of the proposed disentanglement procedure and of the three-phase model. On the other hand, the resistance has a maximum at a field close to the coercivity of phase 2. This effect can be understood considering the large separation between the coercivities of the two phases. Phase 1 reaches saturation, no longer contributing to magnetoresistance, well before the coercive field of phase 2. Phase 2 is associated with the cap layer, which is highly corrugated and possibly non-continuous. The coercivity of this Co layer is therefore likely to be related to a very high disorder of the magnetization vector (including also out-of-plane components) on the electron mean free path scale. The contribution from phase 2 is probably the GMR type, which gives the maximum at the coercive force. The resistivity maximum occurs when the underlayer is already saturated, while in the cap layer the in-plane magnetization is randomly oriented, and a substantial fraction of out-of-plane magnetization may still exist. The agreement between H_{C2} and H_{Max} is slightly worse than that between H_{C1} and $H_{\min}$, possibly because of the concomitant presence of the GMR from nanoparticles and of the OMR. The fields $H_{\min}$ and H_w are shown together in figure 7: their trend with temperature is similar and a linear correlation of the two quantities exists (inset). This is taken as further proof of the existence of a unique physical phenomenon resulting in the magnetoresistive dip we measured.

The analysis of the low-field magnetoresistance dip can be further developed. It is assumed that the AMR signal comes entirely from effects related to the presence of magnetic domains in the demagnetized state of the Co underlayer. Owing to the structural nature of this evaporated layer, characterized by high crystalline disorder induced by thermal evaporation, the local magnetization vector must point along different directions of the layer plane from one region to the other; the magnetic domains have no simple shape and are separated by undulating, non-planar Néel walls [13]; as a consequence, a highly disordered distribution of the magnetization vector in the plane of the layer is expected at the coercive field, even if the magnetization process occurs via Néel wall displacement. Using the standard expression for the AMR [14]:

$$R_{\mathrm{AMR}} = R_{\perp} + \left(R_{\parallel} - R_{\perp}\right)\left\langle \cos^2\theta \right\rangle, \qquad (3)$$

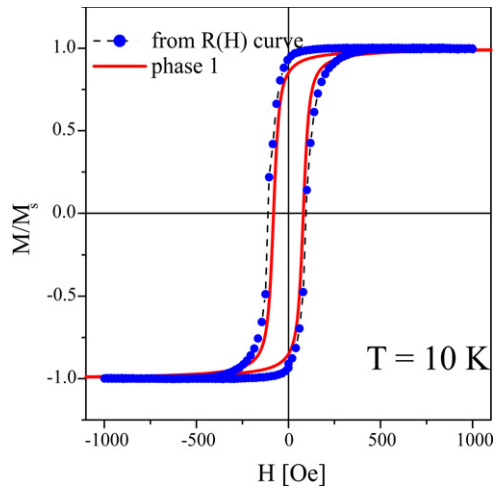

Figure 8. Symbols: $\langle\cos\theta\rangle$ quantity obtained by MR measurements; line: reduced magnetization M/M_{sat} of magnetic phase 1.

where θ is the angle between the local magnetization within a magnetic domain and the common direction of magnetic field and electrical current, it is inferred that $R_{\parallel} \approx R_{1\ \mathrm{kOe}}$ (phase 1 has already attained saturation at this magnetic field, see figure 3(b)) and that $(2/3\ R_{\perp} + 1/3\ R_{\parallel}) \approx R_{H_{\min}}$ (the magnetization is assumed to be almost randomly distributed at $H = H_{\min}$, so that $\langle\cos^2\theta\rangle = 1/3$). As a consequence, it is possible to obtain the variation of $\langle\cos^2\theta\rangle$ with H from the magnetoresistance curve. On the other hand, the magnetization of the underlayer is given by $M(H) = M_s\langle\cos\theta\rangle$, where M_s is the spontaneous magnetization. The following relationship between the first and second moments of $\cos\theta$ can be exploited:

$$\langle\cos^2\theta\rangle = \tfrac{1}{3} + \tfrac{2}{3}\langle\cos\theta\rangle^3 \qquad (4)$$

which is based on random-walk arguments and can be applied to a magnetic system with random or highly disordered distribution of the magnetization vector [15]. As a consequence, electrical resistance data are used to estimate the field behaviour of the reduced magnetization $M/M_s \equiv \langle\cos\theta\rangle$. As an example, $\langle\cos\theta\rangle$ at $T = 10$ K is shown in figure 8. The M/M_s curve of phase 1 alone, as deduced from the fitting procedure of magnetic data at the same temperature, is also shown. The agreement between the two curves is notable, in spite of their totally different origin. We conclude that the low-field resistance dip actually comes from the magnetization process in the Co underlayer, which mainly involves planar rotations of the randomly distributed magnetization vector.

6. Resistor network model and genetic algorithm

A simple resistor network model has been developed to interpret the MR behaviour of the sample. Basically, this resistor network model is developed after the two-current picture widely used to describe conduction properties of spin valves [5]. We modelled the multilayer as the parallel between four resistive elements, one of which plays, however, a negligible role as discussed below (figure 9(a)), including two different GMR-like elements representing the Co cap layer signal R_{cap} and the Co nanoparticles embedded in Sn islands R_{NP}, an AMR contribution coming from Co underlayer R_{under} and a hopping-type Sn sheet resistance R_{hopping}. While the choice of a GMR-like expression is the natural one for the nanoparticle contribution, making the same choice for the cap layer is justified by considering its highly corrugated nature (see figure 9(b)), which is supposed to result in local strains and local anisotropy axes, giving rise to significant magnetic disorder on the nanometre scale. Spin-dependent electron scattering by magnetic inhomogeneity on this scale has been shown to result in a GMR-like effect (termed 'proximity magnetoresistance' [16]).

The transverse resistance of the Sn island-like layer R_{Sn} is also considered in our model, represented as a resistive element put in series with the nanoparticle GMR-like one.

In figure 9(b) simplified examples of the possible conductive paths across the multilayered structure are sketched (it should be remembered that the leads are in electrical contact with the cap layer). The section is cut along the AB line obtained as indicated in the upper part of the figure, where a process of image depth degradation is applied, from left to right, to an FESEM detail in order to obtain a black/white contrast pattern [6]. Path 2 (solid (red) line) is completed

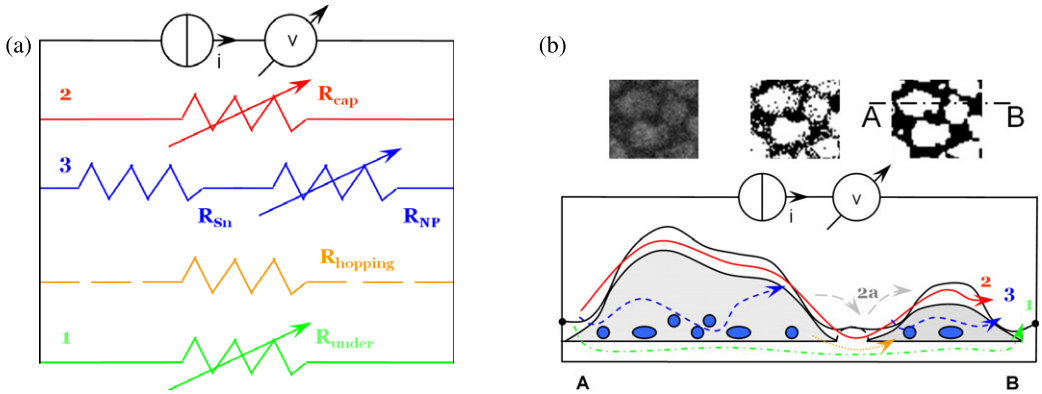

Figure 9. (a) Resistor network model; (b) conduction mechanisms proposed for the multilayered structure (above: detail taken from an FESEM image—see the text; below: sketch of the sectioned multilayer portion across the AB segment, with examples of possible electron conduction paths).

within the corrugated cap layer (phase 2). Path 3 (dashed (blue) line) depicts the case when the electron crosses the interface between an Sn island and the cap layer, and is comprised of both the R_{Sn} and the R_{NP} terms; the electron starts from the cap layer, crosses the interface with the Sn island, travels in the island through the Co nanoparticles (phase 3), crosses again the interface towards the cap layer and ends its path there. Path 1 (dotted–dashed (green) line) is completed within the underlayer (phase 1); the electron starts from the cap layer, crosses either the Sn islands or the direct interface cap layer/underlayer, travels through the underlayer, crosses again the interface towards the external layer and ends its path there.

Excluding the low resistivity paths described above, followed by electrons partly travelling either in the cap layer or in the underlayer, the ideal *in-plane* resistance of the island-like Sn layer should be ascribed to intercluster hopping only (Sn islands constituting a non-percolating system by themselves). The quantity R_{hopping} (related to paths exemplified in figure 9(b) by the (orange) dotted arrow) is therefore expected to be quite high, so that it does not contribute in the parallel circuit.

All conductive paths are in parallel; the in-plane conduction across different Sn islands requires a passage back to the cap layer and falls again in case 2, as discussed above.

Each element resistance is related to the corresponding (normalized) magnetization curve M_{cap}, M_{NP} or M_{under}. Resistive elements have been characterized by two parameters, according to the following equations:

$$\begin{aligned} R_{\mathrm{cap}} &= R_{\mathrm{cap,rand}}\left[1 - a\left(\frac{M_{\mathrm{cap}}}{M_{\mathrm{cap,sat}}}\right)^2\right] \\ R_{\mathrm{NP}} &= R_{\mathrm{NP},H=0}\left[1 - b\left(\frac{M_{\mathrm{NP}}}{M_{\mathrm{NP,sat}}}\right)^2\right] \\ R_{\mathrm{under}} &= cR_{\mathrm{under},\parallel} + \left(R_{\mathrm{under},\parallel} - cR_{\mathrm{under},\parallel}\right) \\ &\quad \times \left(\frac{2}{3}\left|\left(\frac{M_{\mathrm{under}}}{M_{\mathrm{under,sat}}}\right)^3\right| + \frac{1}{3}\right). \end{aligned} \tag{5}$$

The first two lines of equation (5) express the usual GMR of a magnetically inhomogeneous medium and of a nanoparticle system, according to [17]. The fitting parameters contained in equation (5) are three shape parameters (a, b, c) and three scale parameters, the ordered state resistance ($R_{\mathrm{under},\parallel}$), the random-state resistance of the cap layer ($R_{\mathrm{cap,rand}}$) and the zero-field resistance of the nanoparticle element ($R_{\mathrm{NP},H=0}$). Together with R_{Sn}, which is supposed to be invariant with respect to the applied field, the values of these parameters may be assumed to constitute a seven-dimensional phase space limited by a hypercube domain with physically significant chosen borders; within this domain we performed an optimization seek.

Each parameter has been determined by means of a genetic algorithm (GA) [18] in order to obtain the best fit of the overall resistance to the experimental data. Use is made of the magnetization values of the three magnetic phases, as determined through the analysis of section 4. The fitting routine considers a population of different individuals, whose characteristics are stored in 8 chromosomes: 7 chromosomes contain the information concerning the six parameters shown in equation (5). Each one has two genes, i.e. the lower and the upper bound of possible parameter values; when the two bounds are set equal, the parameter is not varied. Each individual has only two varying parameters, in order to easily visualize the fitting error on the third dimension. Since the shape and the scale parameters whose effect is magnetic-field-sensitive constitute separate families, the total number of considered permutations is n^2, where $n = 3$. The chosen population is redundant, so that 16 individuals are used in order to minimize the fitting error (least-squares method). The parameter space is a grid 25×25 wide, so for each generation $625 \times 16 = 10^4$ different resistive configurations are tested. The seventh chromosome contains the information about the exact values of the varying parameters that minimize the difference between individual and experimental measurement and about the error. During the crossover subroutine, the upper and lower bound of the next-generation-individual-parameter are chosen in such a way as to include the best value found in the previous generation; or they extend the fitting interval to include new values (if the best configuration was found in correspondence to the lower/upper bound). The density factor (also called the damping factor) that describes the sampling step for each parameter interval is computed as the difference between the error of the actual individual and the error of the best individual, normalized with respect to the last one: the lower the error, the higher the density. Also, a mutation subroutine is randomly activated in a certain percentage of the simulated configurations in order to explore different positions in the parameter phase space, even though user-defined bounds are respected. Hence chromosomes that have undergone a mutation process may result in a worse individual (poorer fit) but allow the algorithm to cover the entire phase space and overcome the problem of finding a local minimum which is not the absolute minimum. One can choose whether to increase the down-climb within the GA, proceeding towards a local minimum, or to increase the up-climb via a higher mutation probability, thus exploring the phase space within defined bounds. Elitism is introduced in order to speed-up convergence: the best ever individual is copied to the following generations without affecting its parameter values. Only the worst individuals are affected by crossover and mutation.

Figure 10 shows the results of the fitting session after the genetic algorithm has been run for 6000 generations, in the case of the MR curve taken at $T = 10$ K; the resistance values have been normalized and evaluated through equation (5) in the entire magnetic field range (−70 to 70 kOe), using for the magnetization parameters the three modified Langevin curves obtained from the three-phase model and extrapolated to high fields. The model qualitatively reproduces both the high-field trend and the low-field region across the resistive minimum, even if the dip is narrower than experimental data. The resistivity values (at $H = 0$) for the three considered elements are reported in table 1 for two temperatures (10 and 50 K).

Figure 11 shows a logarithmic plot of the three resistance terms defined in equation (5) as functions of the applied field, together with the fitted curve (one branch only); note that both R_{cap} and R_{under} are asymmetrical functions and

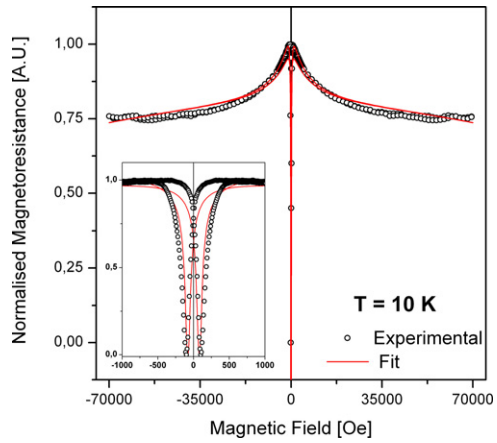

Figure 10. Resistor network output is shown to fit experimental data measured at 10 K in the high-field and low-field region (inset).

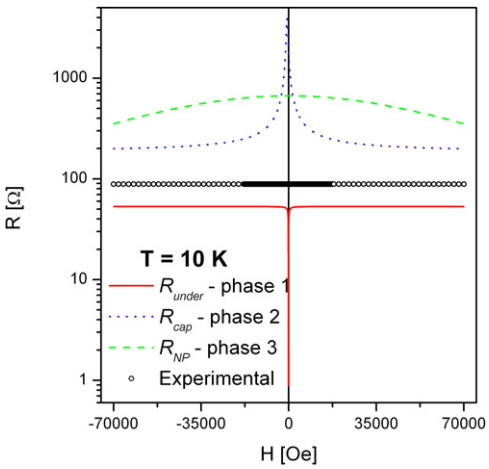

Figure 11. Logarithmic plot of the three resistance terms of the resistor network model at $T = 10$ K; experimental MR curve (one branch only) at the same temperature.

Table 1. Selected resistivity values (at $H = 0$) obtained from the best fit to experimental curves of the resistor network model using the genetic algorithm; for comparison, in the last column the experimental resistivity of an evaporated Co/Cu/Co trilayer is given.

T (K)	ρ_{cap} (Ω m)	ρ_{NP} (Ω m)	ρ_{under} (Ω m)	$\rho_{Co/Cu/Co}$ (Ω m)
10	5.17×10^{-5}	1.99×10^{-7}	1.00×10^{-7}	1.08×10^{-7}
50	2.66×10^{-5}	2.02×10^{-7}	1.01×10^{-7}	1.11×10^{-7}

therefore contribute to the asymmetrical shape of the overall MR curve. On this scale, the low-field features of the actual experimental curve are hidden. The reported values of the resistance terms (in ohms) are obtained by requiring that the resistor network output (which comes in arbitrary units) scales to fit the actual resistance measurements. It should be remarked that the maximum value of the cap layer resistance is almost two orders of magnitude higher than the corresponding value for the underlayer. This applies to electrical resistivities also, because the two layers have comparable thicknesses. As a consequence, we infer that the conduction mechanisms in the two layers are quite different. Such a conclusion is supported by the temperature behaviour of the three resistivities ρ_{cap}, ρ_{under} and ρ_{NP} shown in table 1. It appears that, while both ρ_{under} and ρ_{NP} increase with increasing T, as expected, the opposite happens for ρ_{cap}, indicating a non-metallic behaviour. It can be supposed that electrical conduction in the cap layer takes place through hopping phenomena between adjacent metal islands, as exemplified in figure 9(b) (short-dashed (grey) line indicated as path 2a). The non-continuity of the cap layer is not directly observable by means of the FESEM–EDX spectroscopy technique because of the concurrent, strong signal coming from the continuous Co underlayer. For comparison we report in the last column of table 1 experimental resistivity values found for a Co/Cu/Co evaporated trilayer (see section 4) with a continuous spacer: a conduction regime similar to that of phase 1 is shown.

7. Conclusion

A Co/Sn/Co trilayer with island-like Sn regions has been produced by thermal evaporation of pure metals on an Si substrate. Magnetic and magnetotransport properties were studied at different temperatures. The trilayer exhibits a complex behaviour of both magnetization and magnetoresistance, which contains OMR-, AMR- and GMR-like contributions. Starting from the hysteresis loops measured at different temperatures, a three-phase model has been developed and shown to successfully reproduce the experimental data. We suggest that phase 1 is coincident with the continuous Co underlayer, phase 2 is associated with the rough and corrugated Co cap layer and phase 3 is related to the presence of Co nanoparticles embedded in the Sn islands. Magnetization curves of the three phases obtained from the fitting procedure have been used to implement a simple magnetoresistive network model. The overall magnetoresistance of the circuit was elaborated via a genetic algorithm to fit low-temperature experimental data. The agreement of such a simple model with actual low-temperature MR measurements is rather good; the absolute values and the temperature behaviour of the fitting parameters point to a regular metallic behaviour of both the Co underlayer and the nanoparticulate phase, and to a non-metallic behaviour of the cap layer, possibly related to a non-percolating morphology.

References

[1] Binasch G, Grunberg P, Saurenbach F and Zinn W 1989 *Phys. Rev.* B **39** 4828–30
[2] Baibich M N, Broto J M, Fert A, Nguyen Van Dau F, Petroff F, Etienne P, Creuzet G, Friederich A and Chazelas A 1988 *Phys. Rev. Lett.* **61** 2472–5
[3] Dieny B, Speriosu V S, Metin S, Parkin S S P, Gurney B A, Baumgart P and Wilhoit D M 1991 *J. Appl. Phys.* **69** 4774–9
[4] Yuasa S, Nagahama T, Fukushima A, Suzuki Y and Ando K 2004 *Nat. Mater.* **3** 868–71
Parkin S S P, Kaiser C, Panchula A, Rice P M, Hughes B, Samanth M and Yang S H 2004 *Nat. Mater.* **3** 862–7
[5] Fert A and Bruno P 1994 *Ultrathin Magnetic Structures II* (Berlin: Springer) p 82 and references therein
[6] Chiolerio A, Chiodoni A and Allia P 2008 *Thin Solid Films* at press (doi:10.1016/j.tsf.2008.04.085)
[7] Stranski I N and Krastanov L v 1937 *Akad. Wiss. Wien, Math. Naturw. Kl. Abtlg.* **146** 797

[8] Berger A, Knappmann S and Oepen H P 1994 *J. Appl. Phys.* **75** 5598–600
Tsay J S, Yao Y D, Wang K C, Cheng W C and Yang C S 2002 *J. Appl. Phys.* **91** 8766–8
[9] Chiolerio A, Allia P, Chiodoni A, Pirri F, Celegato F and Coisson M 2007 *J. Appl. Phys.* **101** 123915
[10] Peterson B L, White R L and Clemens B M 2003 *Physica* B **336** 157–61
[11] Skumryev V, Stoyanov S, Zhang Y, Hadjipanayis G, Givord D and Nogues J 2003 *Nature* **423** 850–3
Vargas J M, Gomez J, Zysler R D and Bufera A 2007 *Nanotechnology* **18** 115714
[12] Allia P, Knobel M, Tiberto P and Vinai F 1995 *Phys. Rev.* B **52** 15398–411
[13] Hubert A and Shaefer R 1998 *Magnetic Domains* (Berlin: Springer) p 238
[14] McGuire T R and Potte R I 1975 *IEEE Trans. Magn.* **11** 1018–38
[15] Allia P, Coisson M, Moya J, Selvaggini V, Tiberto P and Vinai F 2003 *Phys. Rev.* B **67** 174412
[16] Allia P, Coisson M, Durin G F, Moya J, Selvaggini V, Tiberto P and Vinai F 2002 *J. Appl. Phys.* **91** 5936–9
[17] Xiao J Q, Jiang J S and Chien C L 1992 *Phys. Rev. Lett.* **68** 3749–52
[18] Holland J H 1992 *Adaptation in Natural and Artificial Systems* (Cambridge, MA: MIT Press) reprinted
Chwastek K and Szczyglowski J 2006 *Math. Comput. Simul.* **71** 206–11